Analysis of the Interaction Among Power Converters Through Their Synchronization Mechanism

Roberto Rosso, *Student Member, IEEE*, Markus Andresen, *Member, IEEE*, Soenke Engelken, *Member, IEEE*, and Marco Liserre, *Fellow, IEEE*

***Abstract*—Recent studies have shown the importance of considering the synchronization mechanism of a grid-connected converter in its stability assessment. Moreover, it is often taken for granted that synchronization units of grid-connected converters operating nearby may interact with each other, but this topic has not yet been deeply investigated in the literature. In this paper, the interaction between synchronization units of grid-connected converters is investigated by means of impedance-based analysis. A multiple-inputs multiple-outputs analysis is required and a stability margin is introduced, based on the calculation of the norm of the equivalent grid impedance and equivalent output admittance of the converter. The sensitivity of the stability margin to parameter variations (e.g., grid impedance, bandwidth of the synchronization loop of each converter) is assessed by means of Monte Carlo simulations. Time-domain simulations as well as experimental results in a laboratory environment using a power hardware-in-the-loop test bench are performed so as to validate the presented frequency-domain analysis.**

***Index Terms*—Infinity-norm, Monte Carlo (MC) simulations, phase-locked loop (PLL) stability, stability margin, synchronization issues.**

I. Introduction

THE synchronization of power electronics converters with the main utility grid has been investigated in the last decades since the number of converter-connected distributed energy resources (DERs) have increased noticeably. Synchronization techniques have been proposed in the literature, both for single-phase as well as for three-phase systems [1]–[5]. The commonly adopted solution is the use of a phase-locked loop (PLL), and the synchronous reference frame (SRF)-PLL is among the most widely proposed techniques in the literature [6]. Although it provides excellent results under nominal-grid conditions, its performance is strongly affected by imbalances and background-harmonic distortion of grid voltages. Solutions have been presented in the literature to partially overcome these

Manuscript received August 10, 2018; revised November 25, 2018 and January 28, 2019; accepted March 7, 2019. Date of publication March 14, 2019; date of current version September 6, 2019. Recommended for publication by Associate Editor F. W. Fuchs. *(Corresponding author: Roberto Rosso.)*

R. Rosso and S. Engelken are with the Department of Control Engineering, ENERCON GmbH, Aurich 26607, Germany (e-mail:

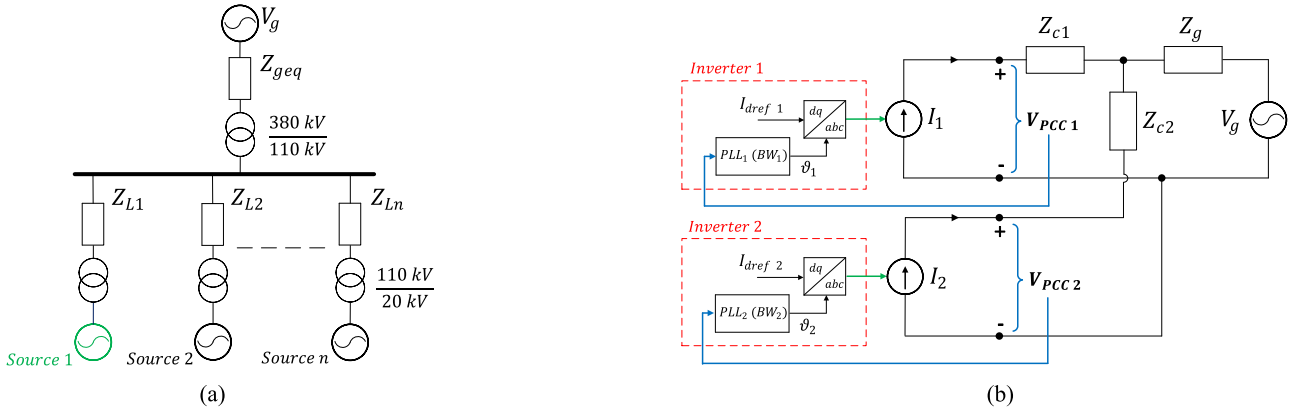

Fig. 1. System under study. (a) Scheme of the system and (b) simplified representation including the control loops for the case of two converters.

a stability margin also provides indications about the robustness with respect to parameter variations. It is also shown that, for the specific application, the defined margin does not suffer from excessive conservatism. Parameters are varied using statistical approaches and Monte Carlo (MC) simulations are performed so as to evaluate their effects on system stability.

This paper is structured as follows. In Section II, the system under study is presented. In Section III, a stability margin is defined, proving its accuracy by means of electromagnetic transient (EMT) time-domain simulations. In Section IV, a statistical approach based on MC simulations is used to assess sensitivity against parameter variations. In Section V, experimental results using a power hardware-in-the-loop (PHIL) test bench are presented, while Section VI is dedicated to the conclusions.

II. Modeling of Parallel Inverters for Studying Synchronization Issues

A. System Under Study

A scheme of the investigated system is reported in Fig. 1(a), while in Fig. 1(b), a simplified representation of the system for the case of only two converters is reported, also showing their control loops. The case of a high-voltage grid is examined, and it can be assumed that each converter represents an aggregated model of many converters having the same characteristics. Since the focus of this paper does not lie on the investigation of the interactions between the PLL and the other control loops of the converter (current control, dc-link voltage/active power control, reactive power control, voltage feed-forward, etc.), which have been already addressed in the literature [14], [15], [20], [21], the converter is assumed to behave as a perfect current source, whose output currents are calculated by transforming the reference currents from the dq to the abc reference frame using the angle estimated by the PLL. This allows isolating the effects of the PLL from the other control loops of the converter, focusing on the interactions among synchronization units of converters operating nearby. This simplification is justified by the difference between the bandwidths of the control loops in question. In fact, the inner current control loop is usually designed so as to be much faster than the synchronization loop, whereas the outer power control loop is generally way slower. For example, hysteresis-band current control (HCC) is among the current control implementations cited in the literature for modeling the performances of real industrial applications [22], which ensures extremely high bandwidth (ideally infinite), whereas the simplification of neglecting the outer control loops has also been adopted in other works, as [12] and [13] among others, where the interactions between inner current control loops and converter output filter of converters operating nearby have been addressed.

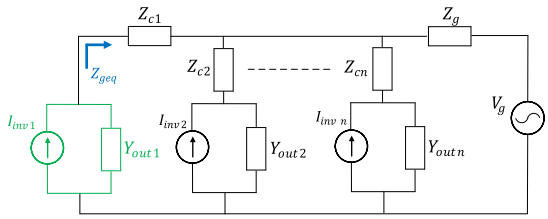

Fig. 2. Equivalent system representation for impedance-based analysis.

It is not necessarily assumed that the converters share the same PCC, but it is considered that they are connected to the same network bus. The grid is therefore represented by its Thévenin equivalent, seen from the bus, whose impedance can be varied so as to emulate a weaker or stronger connection point. The impedances Z_{c1} and Z_{c2}, shown in Fig. 1(b), include the impedance of the medium-voltage/high-voltage transformer of each converter and one of the respective lines Z_{L1} and Z_{L2}. The impedance indicated as Z_g in Fig. 1(b) accounts for the sum of the high-voltage transformer impedance and the equivalent grid impedance Z_{geq}.

B. Equivalent Output Admittance and Grid Impedance

The equivalent system model suitable for impedance-based analysis is shown in Fig. 2. The linearization of the PLL equations has been reported in [20]. However, the calculation of the equivalent grid impedance is slightly different, due to the presence of the impedances between converters. Defining I_{ref1} the reference current of converter 1 and V_g the grid voltage, the

expression of the output current of converter 1 is

$$I_{\text{inv1}}(s) = H(s)[I_{\text{ref1}} + Y_{\text{out1}}(s)V_g] \tag{1}$$

with

$$H(s) = \frac{1}{1 + Z_{\text{geq}}(s)Y_{\text{out1}}(s)}. \tag{2}$$

The equivalent grid impedance $Z_{\text{geq}}(s)$ seen by converter 1 can be calculated as

$$Z_{\text{geq}}(s) = Z_{c1}(s) + \frac{1}{\frac{1}{Z_g(s)} + Y_{o2}(s) + \cdots + Y_{on}(s)} \tag{3}$$

where $Y_{on}(s)$ of the nth converter is obtained from $Z_{cn}(s)$ and $Y_{\text{outn}}(s)$ as follows:

$$Y_{on}(s) = \frac{1}{Z_{cn}(s) + \frac{1}{Y_{\text{outn}}(s)}}. \tag{4}$$

Neglecting the effects of the PLL as that in [12] and [13], the impedances and admittances in (1)–(4) are represented by SISO transfer functions. As in [14], the formulation in dq coordinates is adopted in this paper, in order to consider the effects of the synchronization unit in the analysis. The problem requires a MIMO formulation, and therefore, the converter output admittance and the equivalent grid impedance are indicated in the following using bold characters.

Considering only the PLL and neglecting the other control loops of the converter, the output admittance is simply expressed by the following equation [14]:

$$\mathbf{Y}_{\text{out}}(s) = \begin{bmatrix} 0 & I_q H_{\text{PLL}}(s) \\ 0 & -I_d H_{\text{PLL}}(s) \end{bmatrix} \tag{5}$$

with I_d and I_q indicating, respectively, the d and q component of the converter current I_{inv1} at the operating point, and $H_{\text{PLL}}(s)$ representing the transfer function of the detected angle $\Delta\theta_{\text{PLL}}$ according to a variation of the input q component of the voltage ΔV_q [14], and is derived as follows:

$$H_{\text{PLL}}(s) = \frac{\Delta\theta_{\text{PLL}}(s)}{\Delta V_q(s)} = \frac{\text{LF}(s)}{s + V_d \text{LF}(s)}. \tag{6}$$

V_d in (6) is the d-component of the voltage at the operating point and $\text{LF}(s)$ is the transfer function of the loop filter of the SRF-PLL:

$$\text{LF}(s) = K_p + \frac{K_i}{s} \tag{7}$$

with K_p and K_i proportional and integral gains, respectively. The representation of a generic resistive–inductive impedance in dq-coordinates is given as follows:

$$\mathbf{Z}_{RL}(s) = \begin{bmatrix} sL + R & -\omega L \\ \omega L & sL + R \end{bmatrix}. \tag{8}$$

III. Norm of Impedances for Stability Margin Calculation

In most of the literature dealing with impedance-based analysis, the common approach used for assessing the stability of the system is to apply the Nyquist stability criterion to the product between the equivalent grid impedance $Z_{\text{geq}}(s)$ and the output admittance of the converter $Y_{\text{out}}(s)$ [12], [13]. However, when the PLL equations are included, the system becomes MIMO, and multivariable control system theory should be applied for assessing system stability. The generalized Nyquist criterion has been used for stability assessment [14], [15], [18], [23]. It provides a sufficient and necessary condition and does not suffer from excessive conservatism. However, it does not provide an indication about stability margin in the same way as it does for SISO systems. Therefore, it is not suitable for design purposes and instead, other methods have been proposed in the literature [19], which define a stability margin based on the calculation of the norms of $\mathbf{Y}_{\text{out}}(s)$ and $\mathbf{Z}_{\text{geq}}(s)$. Although a problem formulation suitable for design purposes can be achieved, the resulting margin might suffer from excessive conservatism. Indeed, such methods provide only a sufficient condition and the system might be stable even if their stability requirements are not met. Such methods are based on the small-gain theorem [17], [24]. In fact, the impedance-based stability criterion is based on the observation that (2) resembles the closed-loop transfer function of a negative-feedback control system, where the forward gain is unity and the feedback gain is the so-called return ratio $\mathbf{L}(s) = \mathbf{Z}_{\text{geq}}(s)\mathbf{Y}_{\text{out}}(s)$.

Indicating with $\overline{\sigma}$ the largest singular value, a compact formulation of the small-gain theorem is reported in the following [17].

Theorem 1 (Small-Gain Theorem): Consider a system with a stable loop transfer function $L(s)$. Then, the closed loop system is stable if

$$\|L\|_\infty = \max_\omega \overline{\sigma}(L(j\omega)) < 1. \tag{9}$$

The proof of the theorem is omitted here for the sake of brevity; it can be found in [24]. If (9) is satisfied, the eigenvalues of the return ratio $\mathbf{L}(s)$ will never encircle the point $(-1, j0)$ and system stability is guaranteed. Equation (9) provides a sufficient condition for stability but might be too conservative in some cases; also, due to the fact that for any eigenvalue λ_i of the return ratio, the following relation is valid [25]:

$$|\lambda_i(j\omega)| \le \overline{\sigma}(L, \omega) \quad \forall\omega \in [-\infty, +\infty]. \tag{10}$$

A design-oriented formulation of (9) can be obtained according to Cauchy's inequality for norms:

$$\|\mathbf{L}\|_\infty = \|\mathbf{Z}_{\text{geq}}\mathbf{Y}_{\text{out}}\|_\infty \le \|\mathbf{Z}_{\text{geq}}\|_\infty \|\mathbf{Y}_{\text{out}}\|_\infty. \tag{11}$$

In [19], a stability margin according to (11) has been proposed, which is reported in the following for simplicity:

$$S_{m1} = 20\log\left(\frac{1}{\|\mathbf{Z}_{\text{geq}}\|_\infty \|\mathbf{Y}_{\text{out}}\|_\infty}\right). \tag{12}$$

Such a formulation noticeably increases the conservatism of the calculation. This can be simply demonstrated by observing Fig. 3, where an example of the frequency behavior of the largest singular value of $\mathbf{Y}_{\text{out}}(s)$ for two different PLL bandwidths is shown, namely $f_c = 50$ Hz and $f_c = 100$ Hz. Here, f_c indicates the cutoff frequency of the PLL open-loop transfer function according to [6]. It is evident that the variation of the PLL bandwidth is simply shifting the curve but not modifying

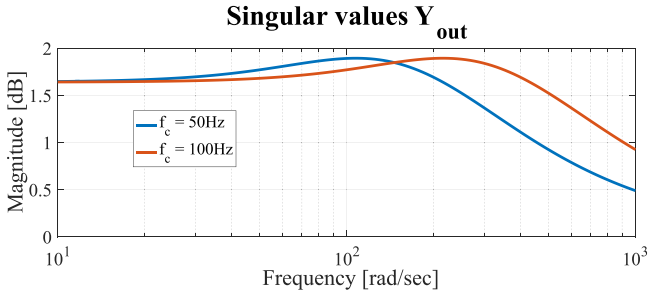

Fig. 3. Example of largest singular values of Y_{out} varying PLL's bandwidth. Blue: $f_c = 50$ Hz. Red: $f_c = 100$ Hz.

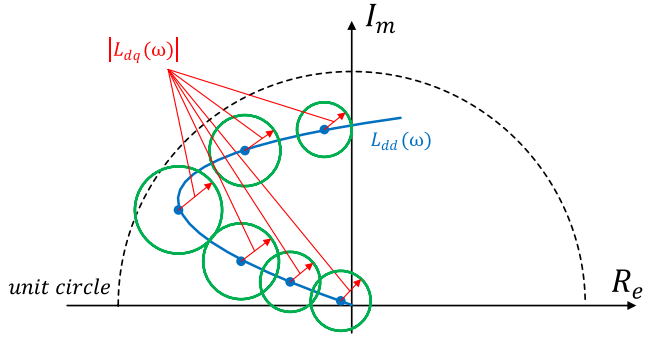

Fig. 4. Graphical explanation of Gerschgorin's theorem.

the largest singular value $\max_\omega \overline{\sigma}(\mathbf{Y}_{\text{out}}(j\omega)) = \|\mathbf{Y}_{\text{out}}\|_\infty$. This implies that, no matter which PLL bandwidth is chosen, the stability margin of the converter will not be affected. This is not realistic and the results might be too conservative.

A. Definition of the Proposed Norm

Let us define the following stability margin S_{m2} as

$$S_{m2} = 20\log\left(\frac{1}{\|\mathbf{L}\|_\infty}\right). \tag{13}$$

In order to evaluate the conservatism of S_{m2}, Gerschgorin's theorem can be applied [19], [23]. The theorem provides a relation between the elements of a matrix and its eigenvalues and is particularly useful for the case of diagonal or strictly dominant diagonal matrices.

Theorem 2 (Gerschgorin's Theorem): Given a square n × n matrix A with entries $a_{ij} \in \{1,...,n\}$, every eigenvalue λ_i of A satisfies

$$|\lambda_i - A_{ii}| \leq \sum_{\substack{j=1 \\ j\neq i}}^{n} |A_{ij}|. \tag{14}$$

Again, the proof of the theorem is omitted here, but can be found in [23]. Generally, eigenvalues are elements of the set of complex numbers $\mathbb{C}$. The theorem states that the ith eigenvalue λ_i of the matrix is limited within a circle centered in the ith diagonal element A_{ii}, whose radius does not exceed in magnitude the sum of the non-diagonal entries in the ith row (Gerschgorin's discs). Expanding the expression of the return ratio $\mathbf{L}(s)$ yields [19]

$$\begin{aligned}\mathbf{L}(s) = \mathbf{Z}_{\text{geq}}(s)\mathbf{Y}_{\text{out}}(s) &= \begin{bmatrix} L_{dd}(s) & L_{dq}(s) \\ L_{qd}(s) & L_{qq}(s) \end{bmatrix} \\ &= \begin{bmatrix} Z_{\text{geq}\,dd}(s) & Z_{\text{geq}\,dq}(s) \\ Z_{\text{geq}\,qd}(s) & Z_{\text{geq}\,qq}(s) \end{bmatrix} \begin{bmatrix} Y_{\text{out}\,dd}(s) & Y_{\text{out}\,dq}(s) \\ Y_{\text{out}\,qd}(s) & Y_{\text{out}\,qq}(s) \end{bmatrix}\end{aligned} \tag{15}$$

and applying Gerschgorin's theorem to $\mathbf{L}(s)$ yields the following inequality for the two eigenvalues λ_1 and λ_2:

$$\begin{cases} |\lambda_1(j\omega) - L_{dd}(j\omega)| \leq |L_{dq}(j\omega)| \\ |\lambda_2(j\omega) - L_{qq}(j\omega)| \leq |L_{qd}(j\omega)|. \end{cases} \tag{16}$$

This means that if $|L_{dq}(j\omega)|$ and $|L_{qd}(j\omega)|$ in (16) are zero or close to zero, the conservatism of S_{m2} due to (10) is practically nullified, since the calculated norm provides a real measure of how far are the eigenvalues from the unit circle. This can be easily understood by observing Fig. 4, where the aforementioned discs are shown. For example, for each ω, the eigenvalue $\lambda_1(j\omega)$ will be located inside a disc centered on $L_{dd}(j\omega)$ and whose radius does not exceed $|L_{dq}(j\omega)|$ in magnitude at the respective frequency. The lower the magnitude of $|L_{dq}(j\omega)|$, the closer will be $\lambda_1(j\omega)$ to $L_{dd}(j\omega)$.

B. Application of the Norm to the Case Under Study

In the following, the norm criterion presented in the previous section is adopted to evaluate the stability of the system and the results are compared to the eigenvalue analysis. Let us consider the case of three converters and assume that initially the converters operate in parallel. Each converter injects its rated active power, whereas no reactive power is injected. The rated power of each converter is calculated as follows:

$$P_{\text{rated}} = \frac{S_{\text{sc}}}{N_{\text{inv}}\,\text{SCR}} \tag{17}$$

where S_{sc} is the short-circuit power of the grid at the bus of interest, SCR the short-circuit ratio and N_{inv} the number of inverters. Subsequently, additional impedances between the converters and the connection bus are introduced, namely Z_{c1}, Z_{c2}, and Z_{c3} in Fig. 2, which are set to one-third of the corresponding grid impedance Z_g. The SCR of the grid and the bandwidth of the first PLL are varied within the ranges SCR = [1.5 ; 3.5] and f_{c1} = [50 ; 300], respectively, whereas the bandwidths of the second and third PLL have been maintained constant to f_{c2} = 100 Hz and $f_{c3} = 50$ Hz. The results obtained from the analysis are reported in Figs. 5 and 6. The maps shown in Figs. 5(a) and 6(a) have been obtained by observing the eigenvalues of (2). The yellow areas represent stable operating regions, while the blue areas are the unstable ones. In Figs. 5(b) and 6(b), the stability margin calculated according to (13) is plotted. In Table I, the parameters for the simulations are shown, where impedances with resistive–inductive behaviors have been considered.

It can be clearly seen that the borders between stable and unstable operating regions match with both calculations. The explanation for this accurate match can be obtained by observing

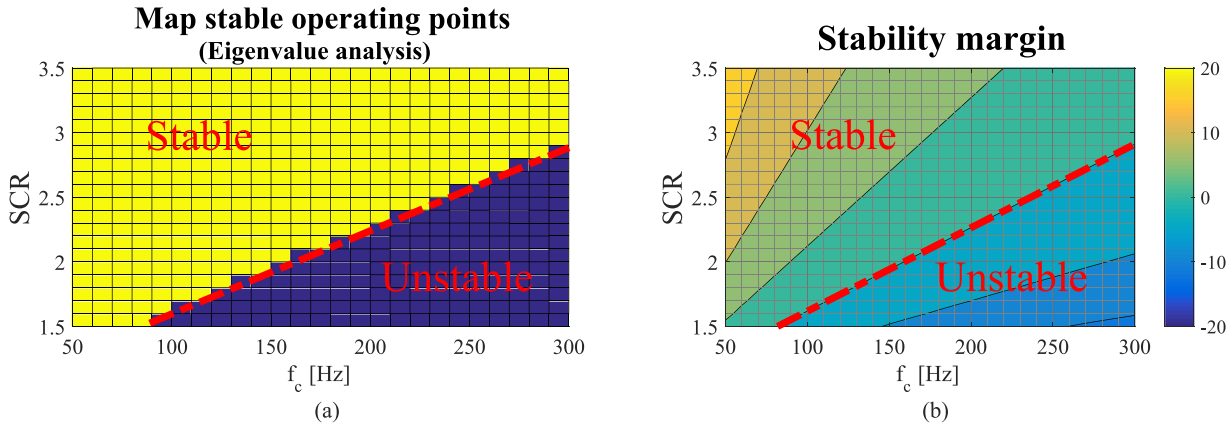

Fig. 5. Converters in parallel. (a) Eigenvalue analysis: (yellow) stable operating points, (blue) unstable ones. (b) Stability margin according to (13).

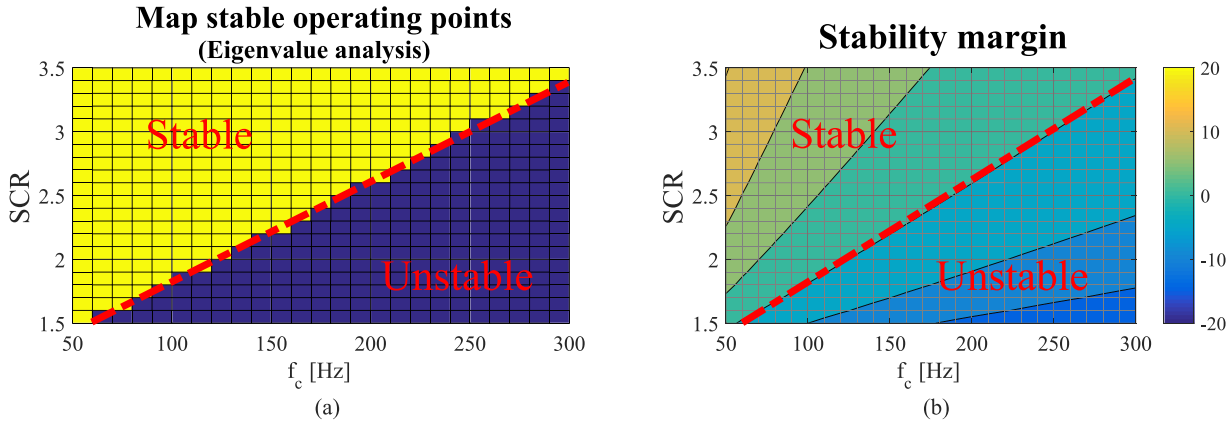

Fig. 6. Converters with additional impedances. (a) Eigenvalue analysis: (yellow) stable operating points, (blue) unstable ones. (b) Stability margin according to (13).

TABLE I
SIMULATION PARAMETERS

Description	Symbol	Value
Grid Short circuit power	S_{sc}	100 MVA
Grid line-to-line voltage	V_{LL}	110 kV (rms)
X/R grid impedance ratio	X/R	10
Rated grid frequency	f_g	50 Hz
Inductance connection impedance	L_c	$L_g/3$
Resistance connection impedance	R_c	$R_g/3$

the return-ratio $\mathbf{L}(s)$ for the particular case under study. If only the synchronization unit is considered for each converter, the resulting $\mathbf{Y}_{\text{out}}(s)$ is given by (5), and therefore,

$$\mathbf{L}(s) = \begin{bmatrix} 0 & Z_{\text{geq}\,dd}(s)Y_{\text{out}\,dq}(s) + Z_{\text{geq}\,dq}(s)Y_{\text{out}\,qq}(s) \\ 0 & Z_{\text{geq}\,qd}(s)Y_{\text{out}\,dq}(s) + Z_{\text{geq}\,qq}(s)Y_{\text{out}\,qq}(s) \end{bmatrix}. \tag{18}$$

Solving the characteristic equation of (18), it is evident that the eigenvalues of the matrix are simply $\lambda_1 = 0$ and $\lambda_2 = L_{qq}(s)$, meaning that the solutions coincide with the diagonal elements of $\mathbf{L}(s)$. In order to assess the conservatism of the norm calculated in (13), $L_{dq}(j\omega)$ and $L_{qq}(j\omega)$ are shown in Fig. 7 for the case with SCR $= 3$ and $f_{c1} = 310$ Hz, with and without additional impedances. It can be noticed that the element of (18)

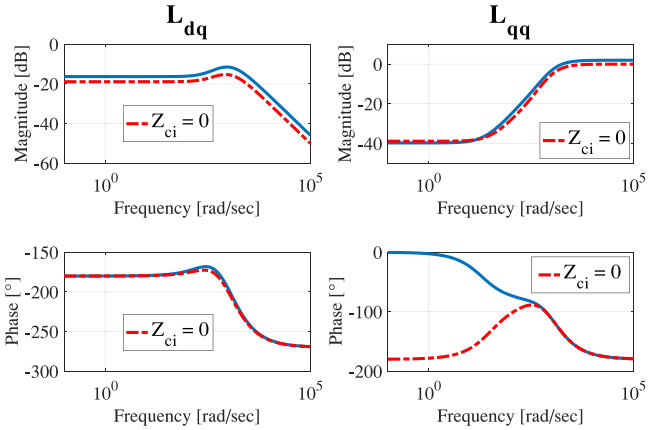

Fig. 7. L_{dq} and L_{qq}. Red dashed: without impedance between converters. Continuous-blue: considering impedances between converters.

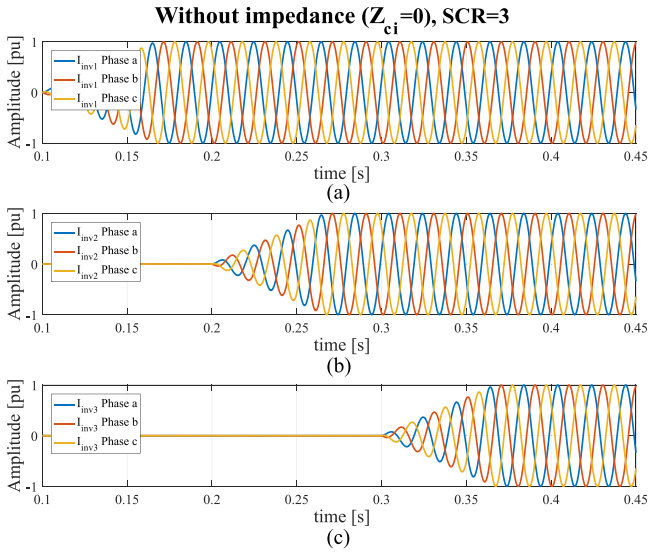

Fig. 8. Simulation results: f_{c1} from 240 to 250 Hz at $t = 0.4$ s, $f_{c2} = 100$ Hz, $f_{c3} = 50$ Hz, $Z_{ci} = 0$, SCR $= 3$. (a) Currents' inverter 1. (b) Currents' inverter 2. (c) Currents' inverter 3.

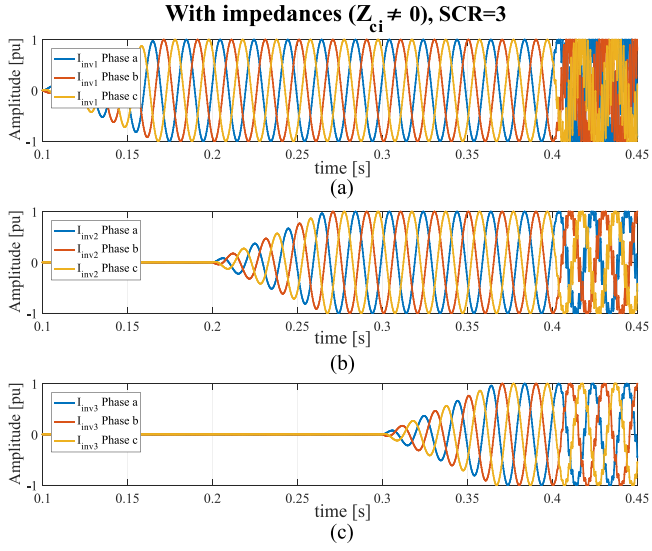

Fig. 9. Simulation results: f_{c1} from 240 to 250 Hz at $t = 0.4$ s, $f_{c2} = 100$ Hz, $f_{c3} = 50$ Hz, $Z_{ci} \neq 0$, SCR $= 3$. (a) Currents' inverter 1. (b) Currents' inverter 2. (c) Currents' inverter 3.

with the largest magnitude is represented by $L_{qq}(j\omega)$, whereas $|L_{dq}(j\omega)|$ is always limited below -10 dB over the whole considered frequency range. The following equation yields from (16):

$$\begin{cases} |L_{dq}(j\omega)| \approx 0 \Rightarrow |\lambda_1(j\omega) - L_{dd}(j\omega)| = 0 \\ |L_{qd}(j\omega)| = 0 \Rightarrow |\lambda_2(j\omega) - L_{qq}(j\omega)| = 0 \end{cases} \tag{19}$$

and therefore, the peak of the largest singular value of $\mathbf{L}(s)$ always corresponds to the infinity norm of $L_{qq}(j\omega)$, and consequently of $\lambda_2(j\omega)$

$$\|\mathbf{L}\|_\infty = \|L_{qq}\|_\infty = \|\lambda_2\|_\infty. \tag{20}$$

This proves that adopting (13) for the calculation of the stability margin of the system, always provides a real estimation of the minimum distance between the only eigenvalue different from zero and the unit circle over the whole frequency range of interest, and precisely from the critical point $(-1, j0)$, as can be deduced from Fig. 7.

C. Simulation Results

In order to validate the performed analysis, the system under study has been simulated in MATLAB/Simulink/PLECS. According to the results shown in Figs. 5 and 6, for SCR $=$ 3 with the converters operating in parallel, f_{c1} has to be increased to approximately 310 Hz to cause instability, whereas when the impedance between the converters is included, a value of $f_{c1} >$ 250 Hz is already critical for the system. Fig. 8 shows simulation results for the case when the converters are operating in parallel. The PLL parameters of inverter 2 and 3 have been chosen such that $f_{c2} = 100$ Hz and $f_{c3} = 50$ Hz. The current of each converter is gradually increased until its rated value is reached and at time $t = 0.4$ s, the parameters of the first PLL are modified such that the resulting bandwidth switches from $f_{c1} = 240$ Hz to $f_{c1} = 250$ Hz. In Fig. 8, simulated currents' waveforms when the converters are operating in parallel are shown, whereas in Fig. 9, simulation results when the impedances are introduced are reported. Time-domain simulations confirm the results predicted by the frequency-domain analysis.

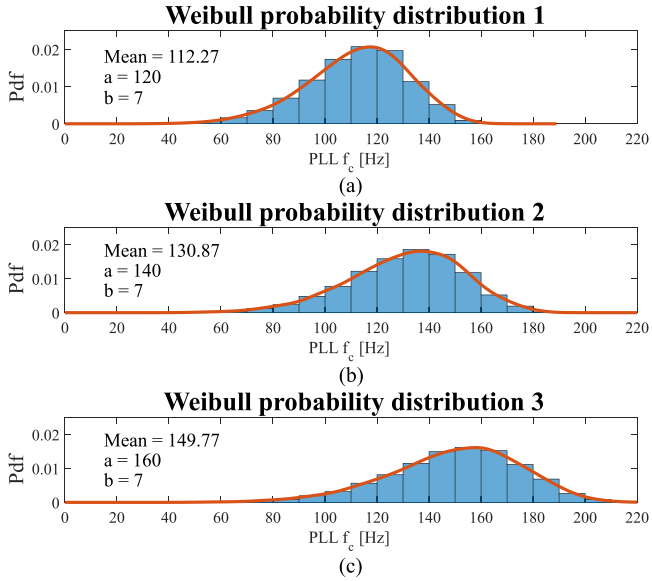

Fig. 10. Probability distribution functions of PLLs bandwidths. (a) Distribution 1. (b) Distribution 2. (c) Distribution 3.

IV. MC Analysis

In the previous section, a stability margin for a MIMO system was defined, and it was demonstrated that for the particular system under study, it does not suffer from excessive conservatism. MC methods are probabilistic approaches based on simulations, which represent an efficient way for sensitivity assessment. They

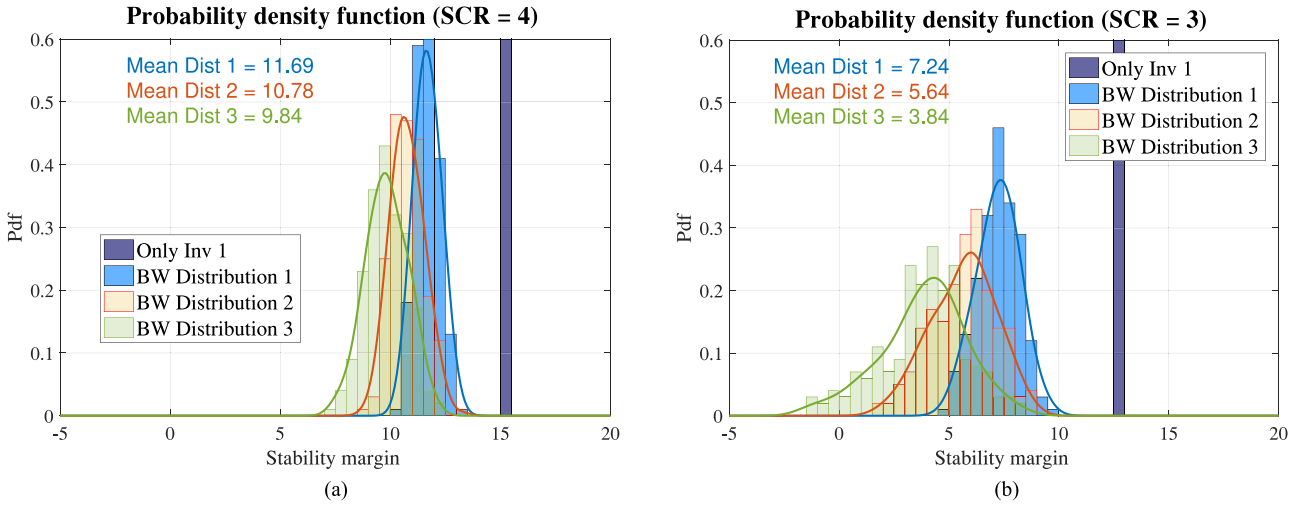

Fig. 11. Simulation results. (a) SCR = 4. (b) = SCR = 3. Violet bars: only Inverter 1 in operation. Blue bars: pdf from Weibull distribution 1. Blue line: pdf fitting from Weibull distribution 1. Red bars: pdf from Weibull distribution 2. Red line: pdf fitting from Weibull distribution 1. Green bars: pdf from Weibull distribution 3. Green line: pdf fitting from Weibull distribution 3.

explore the behavior of the system for a broad range of possible scenarios. Furthermore, they are particularly suitable for investigating possible interactions between system variables, which are very complicated to assess analytically. This approach has been extensively used in the literature for different purposes, both by the power electronics community, for predicting the lifetime of power electronics devices [26], [27], and by the power systems community, to assess the risks of operation [28]. In this paper, an MC analysis is applied to the system under study to investigate the effects of parameters' variations on system stability.

A. Simulation Results

In the following, we will focus on the interaction between synchronization units of converters operating nearby varying grid conditions and PLL bandwidths. This is done with a statistical approach, defining probability density functions (pdfs) for the bandwidths of the PLLs, while varying the SCR of the grid to determined values. The Weibull distribution is very versatile and is widely used in statistical analysis. Compared to a standard normal distribution, data are not necessarily symmetrically distributed around the mean value. In Fig. 10, three Weibull distributions are shown, which will be used for the analysis. Their pdfs are expressed as follows [28]:

$$f(x) = \frac{b}{a}\left(\frac{x}{a}\right)^{b-1} e^{-\left(\frac{x}{a}\right)^{b}} (0 \leq x < \infty\,;\, a, b > 0) \qquad (21)$$

where a is the so-called scale parameter and b is the shape parameter. The scale parameter a is varied in order to shift the distribution on the x-axis, while b is maintained constant. This has the effect of shifting the mean value of the distribution, while stretching out the pdf. The parameters of the three distributions of Fig. 10 are reported in the respective plots, along with their resulting average values. The red lines represent a fit of the resulting pdfs using a kernel distribution.

TABLE II
MC SIMULATION PARAMETERS

Description	Symbol	Value
Grid Short circuit power	S_{sc}	100 MVA
Grid line-to-line voltage	V_{LL}	110 kV (rms)
X/R grid impedance ratio	X/R	10
Rated grid frequency	f_g	50 Hz
Number of inverters	N_{inv}	3
Inductance of additional impedance	L_c	0.045 pu
Resistance of additional impedance	R_c	0.006 pu

The number of inverters is set to three, while $X/R = 10$. Impedances between converters are also included, representing those of the corresponding transformers plus connection lines between the transformer and the network bus. For simplicity, those values are maintained fixed and equal for the three inverters. Two cases with different SCR are considered, namely SCR = 4 and SCR = 3. Random values are drawn from each distribution and 200 simulations for each of the distributions shown in Fig. 10 have been performed. The results are shown in Fig. 11, while simulation parameters are reported in Table II. The violet lines represent the calculated stability margin of the system when only one converter is in operation, injecting its rated power and with $f_{c1} = 100$ Hz, while it is assumed that the other two converters are switched OFF. Subsequently, random values out of the defined distributions are taken for the PLLs of the other two converters, while $f_{c1} = 100$ Hz. In Fig. 11(a) and (b), results for SCR = 4 and SCR = 3 are shown, respectively. PDFs of the corresponding stability margins are shown together with their average values. A curve fit of the resulting pdfs is also shown in Fig. 11, obtained using a Kernel distribution.

The resulting pdfs have lower average values when increasing the bandwidth of the PLLs in both cases. For SCR = 3, not only the average value of the pdfs decreases, but each distribution is wider spread in the x-axis when compared to the case of SCR = 4. This clearly shows that the effects of the interactions

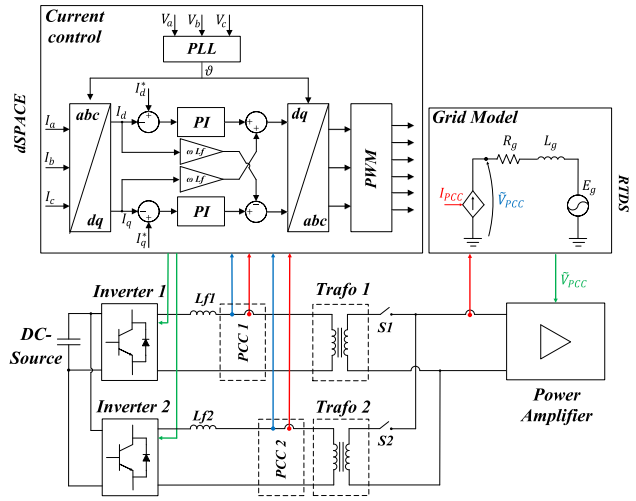

(a)

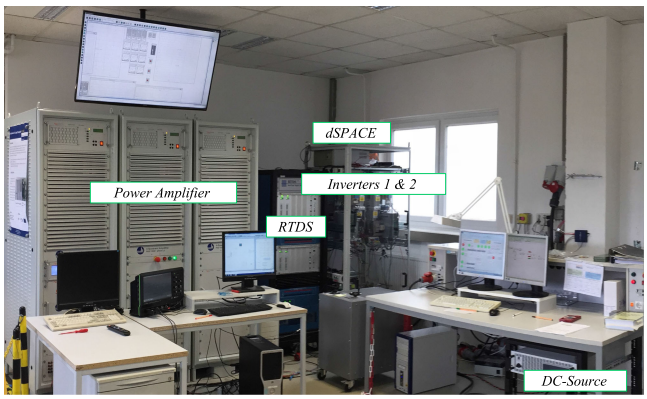

(b)

Fig. 12. (a) Scheme of the laboratory setup used for the tests. (b) Picture of the laboratory setup.

between converters become more accentuated when increasing the impedance of the grid.

V. Experimental Results

A. Description Laboratory Setup

In order to validate the analysis presented in this paper, experimental tests have been performed. The laboratory setup used for the tests is shown in Fig. 12. Two converters Danfoss Series FC-302, with 4 kVA rated power, operating with a switching frequency of 10 kHz and equipped with an output inductive filter have been used to emulate the current sources. In order to reproduce conditions similar to the ones investigated in this paper, the current control of each converter has been implemented using PI controllers, whose parameters k_{pi} and k_{ii} have been tuned according to the technical optimum technique [2]. Furthermore, no voltage feed-forward has been implemented and only an inductive filter has been used.

TABLE III
Parameters Experimental Setup

Description	Symbol	Value
Inverters 1 and 2 rated powers	$S_{n1} = S_{n2}$	4 kVA
Grid line-to-line voltage	V_{LL}	400 V (rms)
Rated grid frequency	f_g	50 Hz
Filter inductance Inv. 1 and 2	$L_{f1} = L_{f2}$	5.2 mH
Impedance Trafo 1 and 2	$L_{T1} = L_{T2}; R_{T1} = R_{T2}$	1.5 mH; 1 Ω
Simulated grid inductance	L_g	5 mH
Simulated grid resistance	R_g	0.2 Ω
DC-Link voltage	V_{dc}	750 V
Converter switching frequency	f_s	10 kHz
Proportional gain current control	K_{pi}	16.7
Integral gain current control	K_{ii}	1500

TABLE IV
Stability Limits

Case	S1	S2	measurements	analytical
1	closed	open	$f_c \approx$1060 Hz	$f_c =$1150 Hz
2	closed	closed	$f_c \approx$600 Hz	$f_c =$ 655 Hz

Each converter is equipped with an additional transformer, in order to provide galvanic isolation. The point of connection of each converter is defined as the voltage at the primary side of the respective transformer. The control algorithms of the two converters have been implemented in a dSPACE control Desk DS1202 MicroLabBox. A 4-quadrant linear power amplifier PAS 15000 from Spitzenberger & Spies (single-phase rated power 15 kVA, total three-phase rated power 45 kVA) has been used as a grid emulator. A virtual inductive–resistive grid has been simulated in real time using a real-time digital simulator (RTDS), which measures the total currents injected by the converters and calculates the corresponding grid voltages of the ideal grid with a time step of 50 μs. The simulated voltages in RS-CAD (simulation software used by the RTDS simulator) are then fed to the power amplifier, which produces the scaled value of the simulated grid voltages at its terminal. Parameters of the experimental setup are listed in Table III.

B. Experimental Results

Two different conditions have been tested. Each converter has been controlled to inject only a d-component of the current $I_d =$ 7 A, corresponding to a value of $P \approx$ 3.4 kW. For each test, the bandwidths of the PLLs were increased simultaneously until instability was reached. In Table IV, the PLL cross-over frequencies causing the instability in the two examined cases are reported and compared to the ones obtained analytically. In the first case, when only one converter is in operation, the bandwidth needed to be increased to an incredibly high value over 1 kHz, in order to cause instability. In the second case, in which the two converters simultaneously inject the same amount of power, a PLL tuning corresponding to $f_c \approx$ 600 Hz caused instability. The critical PLL bandwidths calculated analytically show the same trend as that measured experimentally. In Fig. 13, current waveforms during the transition from stable to unstable operation are

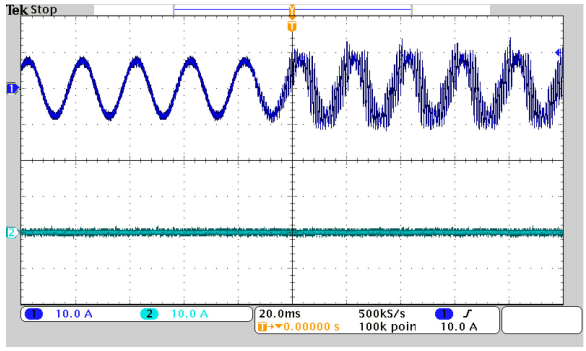

(a)

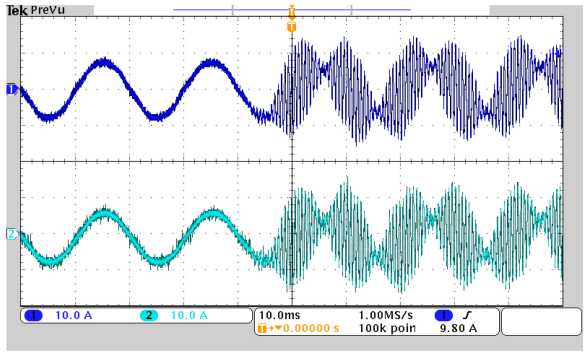

(b)

Fig. 13. Oscilloscope measurements. Blue: phase a current of converter 1. Cyan: phase a current of converter 2. (a) Case 1. (b) Case 2.

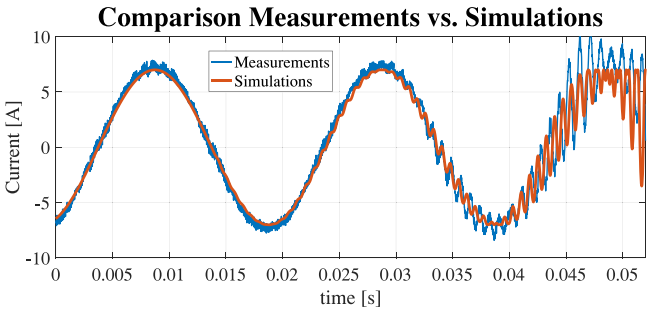

Fig. 14. Case 1: zoom transition from stable to unstable operation. Blue: measurements. Red: simulations.

shown, whereas Fig. 14 shows the comparison between measured and simulated current waveforms of the converter during the transition from stable to unstable operation in Case 1.

Simulation results have been carried out using the simulation model implemented in MATLAB/Simulink/PLECS already utilized in Section III-B for the plots in Figs. 8 and 9, adapting system parameters to the laboratory setup. The critical f_c for the simulation as well as for the measurements correspond to the values reported in Table IV.

Even though a perfect match between the two waveforms shown in Fig. 14 is not achieved, the comparison demonstrates that the instability effects observed in simulations have been reproduced by means of the laboratory setup. Additionally, the values reported in Table IV confirm the trend of the stability border between stable and unstable regions calculated analytically assuming the perfect current source behavior of the converter, namely the drastic reduction of the highest achievable bandwidth of the PLL when the second converter is in operation.

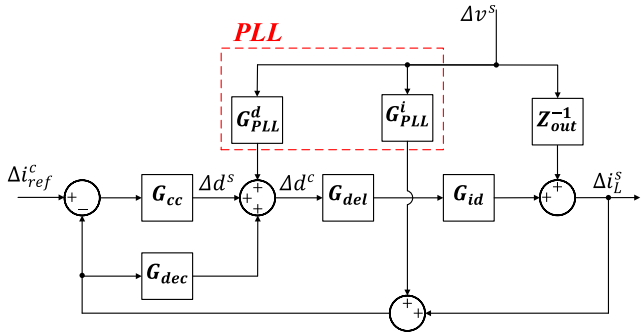

Fig. 15. Small-signal model of the inverter including the effects of the inner current control loop with PI.

C. *Effects of the Inner Current Control Loop*

Several control methods have been proposed in the literature, in order to implement current control loops of power converters [29]. Beside the standard control techniques based on PI or PR controllers, other non-linear control techniques have been proposed. Those include the already mentioned HCC, which directly controls the states of the converter without the need of a modulation signal, sliding mode control [30], or model-based predictive control [29], [31], to name but a few. In this section, the effects of the inner current control loop implemented by means of PI controllers, as in the laboratory setup, are investigated analytically. For this purpose, the approach presented in [14] has been adopted and briefly explained in the following.

In Fig. 15, the small-signal model of the converter including the effects of the PLL and of the inner current control loop implemented using PI controllers is shown. Seven 2×2 transfer function matrices appear in Fig. 15, namely $\mathbf{G}^i_{\mathrm{PLL}}(s)$ and $\mathbf{G}^d_{\mathrm{PLL}}(s)$ accounting for the effects of the PLL on the measured currents and on the duty-cycle, respectively, the matrices related to the current control $\mathbf{G}_{cc}(s)$ and $\mathbf{G}_{\mathrm{dec}}(s)$, the transfer function matrix $\mathbf{G}_{\mathrm{del}}(s)$ reproducing the effects of the delay introduced by the modulation and the digital control, the transfer function matrix $\mathbf{G}_{id}(s)$ between the duty-ratio and the converter output filter current, and $\mathbf{Y}_{\mathrm{ol}}(s)$ representing the effects of the converter open-loop output admittance. The matrices are reported in the following for sake of clarity, whereas their derivation has been thoroughly described in [14], and therefore is not repeated here.

The transfer function matrix $\mathbf{G}^d_{\mathrm{PLL}}(s)$ represents the effects of the PLL on the duty-cycle of the converter and is defined as

$$\mathbf{G}^d_{\mathrm{PLL}}(s) = \begin{bmatrix} 0 & -D_q H_{\mathrm{PLL}}(s) \\ 0 & D_d H_{\mathrm{PLL}}(s) \end{bmatrix} \tag{22}$$

where $H_{\mathrm{PLL}}(s)$ has already been reported in (6), and D_d and D_q are the d and q components of the duty-ratio at the operating point, respectively. $\mathbf{G}^i_{\mathrm{PLL}}(s)$ corresponds to the matrix already

defined in (5), representing in this case the effects of the PLL on the measured converter currents. The transfer function matrices $\mathbf{G}_{cc}(s)$ and $\mathbf{G}_{\text{dec}}(s)$ related to the current control are reported as follows:

$$\mathbf{G}_{cc}(s) = \begin{bmatrix} \frac{sK_{pi}+K_{ii}}{s} & 0 \\ 0 & \frac{sK_{pi}+K_{ii}}{s} \end{bmatrix} \tag{23}$$

$$\mathbf{G}_{\text{dec}}(s) = \begin{bmatrix} 0 & -\frac{3\omega L_f}{V_{\text{dc}}} \\ \frac{3\omega L_f}{V_{\text{dc}}} & 0 \end{bmatrix} \tag{24}$$

with ω representing the nominal grid frequency, L_f the filter inductance, and V_{dc} the value of the converter dc-link voltage. Defining $T_{\text{del}} = 1.5/f_s$, $\mathbf{G}_{\text{del}}(s)$ is given by

$$\mathbf{G}_{\text{del}}(s) = \begin{bmatrix} \frac{1-s(T_{\text{del}}/2)}{1+s(T_{\text{del}}/2)} & 0 \\ 0 & \frac{1-s(T_{\text{del}}/2)}{1+s(T_{\text{del}}/2)} \end{bmatrix}. \tag{25}$$

$\mathbf{Y}_{\text{ol}}(s)$ is defined as the open loop output admittance of the converter without considering the control, namely

$$\mathbf{Y}_{\text{ol}}(s) = \frac{1}{(sL_f + R_f)^2 + (\omega L_f)^2} \begin{bmatrix} sL_f + R_f & \omega L_f \\ -\omega L_f & sL_f + R_f \end{bmatrix} \tag{26}$$

with L_f and R_f representing the inductive and resistive components of the filter impedance, respectively. $\mathbf{G}_{id}(s)$ is the transfer function between the duty-ratio of the converter and the inductor current, given by

$$\mathbf{G}_{id}(s) = -V_{\text{dc}}\mathbf{Y}_{\text{ol}}(s). \tag{27}$$

The equivalent output impedance of the converter is calculated as

$$\begin{aligned} \mathbf{Z}_{oCC}(s) = \Big(& \mathbf{Y}_{\text{ol}}(s) + \mathbf{G}_{id}(s)\mathbf{G}_{\text{del}}(s)\mathbf{G}^{d}_{\text{PLL}}(s) \\ & + \mathbf{G}_{id}(s)\mathbf{G}_{\text{del}}(s)\big(-\mathbf{G}_{ci}(s) + \mathbf{G}_{\text{dec}}(s)\big)\mathbf{G}^{i}_{\text{PLL}}(s)\Big)^{-1} \\ & \times \Big(\mathbf{I} + \mathbf{G}_{id}(s)\mathbf{G}_{\text{del}}(s)\big(\mathbf{G}_{ci}(s) - \mathbf{G}_{\text{dec}}(s)\big)\Big). \end{aligned} \tag{28}$$

System stability can be investigated using the GNC, as that in [14] and [15], or simply observing the eigenvalues of (2). The following two aspects should be however highlighted.

1) Although a norm can still be calculated, the conditions proving the non-conservatism of the results are not fulfilled and the calculation does not provide any reliable indication about the real system stability margin. Therefore, the MC analysis performed in the previous section of this paper cannot be performed in this case, unless another calculation of stability margin for MIMO systems is adopted.
2) The calculation of the converter output admittance noticeably increases the computational burden and it might become troublesome. The use of symbolic software for the calculation of the matrices of interest might represent a suitable approach. In this paper, the symbolic toolbox of MATLAB has been used and the system parameters are then substituted in order to calculate the eigenvalues of (2).

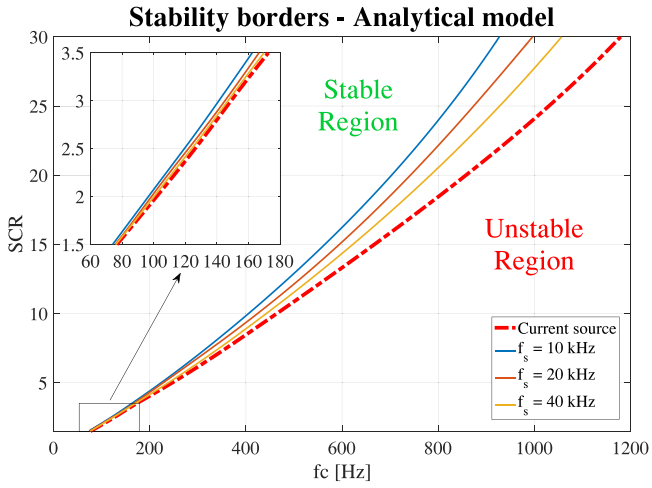

Fig. 16. Stability borders calculated analytically. Continuous-blue: $f_s = 10$ kHz. Continuous-orange: $f_s = 20$ kHz. Continuous-yellow: $f_s = 40$ kHz. Dotted-red: ideal current source.

In Fig. 16, the borders between stable and unstable regions are calculated analytically observing the location of the eigenvalues of (2). The red-dashed line represents the stability border calculated considering a perfect current source behavior of the converter, namely the highest achievable bandwidth of the current control loop. The curve is compared to the borders calculated considering the effects of the inner current control loop implemented using PI controllers tuned according to the technical optimum technique, assuming different values of the converter switching frequency f_s, namely $f_s = 10$ kHz (continuous blue line), $f_s = 20$ kHz (continuous orange line), and $f_s = 40$ kHz (continuous yellow line). The range of the SCR on the y-axis goes from 1.5 to 30, the latter corresponding to the equivalent grid SCR with the parameters shown in Table III, and when the converter injects $I_d = 7$ A.

The analysis shows that, compared to the ideal current source condition, instability tends to occur at lower PLL bandwidths when the PI inner current control loop is implemented. It becomes also evident that increasing the converter switching frequency, the borders calculated under the PI control conditions tend to approach the red-dotted line. Although a punctual match between measurements and analytical calculations is not achieved, this trend has been also confirmed experimentally. In fact, measurements show that the PLL bandwidth causing instability was for both measured cases below the theoretical limit calculated considering the perfect current source behavior. On the top left-hand side of Fig. 16 a zoom into the region where SCR $= [1.5\,;3.5]$ is shown. It reveals that the discrepancy between the investigated cases becomes negligible under the weak grid conditions addressed in this paper.

VI. Conclusion

In this paper, the interactions among synchronization units of converters operating nearby have been studied by means of

an MC-based analysis. Due to the MIMO formulation of the problem, a suitable stability margin has been first introduced, in order to quantify the effects of parameter variation on the stability margin of the system. It has been proven that, for the specific case under study, the defined margin does not suffer from excessive conservatism, providing therefore an accurate estimation of the real stability limit of the system. The defined margin has been adopted for an MC-based analysis, which reveals that the maximum achievable bandwidth of a PLL has strict limitations, especially for operation at low grid SCR and in the presence of other PLL-based converters operating nearby. In fact, decreasing the grid SCR at the connection point, not only the highest achievable bandwidth of the synchronization unit is compromised, but the interactions among synchronization units of converters operating nearby become stronger. The results of the performed analysis have been validated through EMT simulations and experimental tests in a laboratory environment using a PHIL test bench.

REFERENCES

[1] P. C. R. E. Best, *Phase Locked Loops: Design, Simulation and Applications*. New York, NY, USA: McGraw-Hill, 1999.

[2] R. Teodorescu, M. Liserre, and P. Rodriguez, *Grid Converters for Photovoltaic and Wind Power Systems.* Hoboken, NJ, USA: Wiley, 2011.

[3] P. Rodriguez, J. Pou, J. Bergas, J. I. Candela, R. P. Burgos, and D. Boroyevich, "Decoupled double synchronous reference frame PLL for power converters control," *IEEE Trans. Power Electron.*, vol. 22, no. 2, pp. 584–592, Mar. 2007.

[4] T. Thacker, D. Boroyevich, R. Burgos, and F. Wang, "Phase-locked loop noise reduction via phase detector implementation for single-phase systems," *IEEE Trans. Ind. Electron.*, vol. 58, no. 6, pp. 2482–2490, Jun. 2011.

[5] F. D. Freijedo, A. G. Yepes, O. Lopez, P. Fernandez-Comesana, and J. Doval-Gandoy, "An optimized implementation of phase locked loops for grid applications," *IEEE Trans. Instrum. Meas.*, vol. 60, no. 9, pp. 3110–3119, Sep. 2011.

[6] F. D. Freijedo, J. Doval-Gandoy, O. Lopez, and E. Acha, "Tuning of phase-locked loops for power converters under distorted utility conditions," *IEEE Trans. Ind. Appl.*, vol. 45, no. 6, pp. 2039–2047, Nov. 2009.

[7] P. C. Krause, O. Wasynczuk, S. D. Sudhoff, and S. Pekarek, *Analysis of Electric Machinery and Drive Systems*, 3rd ed. Piscataway, NJ, USA: Wiley-IEEE Press, 2013.

[8] A. Johnson, "GC0100—Fast fault current injection, fault ride through and banding." 2017. [Onilne]. Available: https://www.nationalgrideso.com

[9] "Expert workgroup on fast fault current injection – Terms of reference." 2018. [Online]. Available: https://www.nationalgrideso.com

[10] R. D. Middlebrook, "Input filter considerations in design and application of switching regulators," in *Proc. Conf. IEEE Ind. Appl. Soc. Annu. Meeting*, 1976, pp. 366–382.

[11] J. Sun, "Impedance-based stability criterion for grid-connected inverters," *IEEE Trans. Power Electron.*, vol. 26, no. 11, pp. 3075–3078, Nov. 2011.

[12] X. Wang, F. Blaabjerg, and W. Wu, "Modeling and analysis of harmonic stability in an AC power-electronics-based power system," *IEEE Trans. Power Electron.*, vol. 29, no. 12, pp. 6421–6432, Dec. 2014.

[13] X. Wang, F. Blaabjerg, M. Liserre, Z. Chen, J. He, and Y. Li, "An active damper for stabilizing power-electronics-based AC systems," *IEEE Trans. Power Electron.*, vol. 29, no. 7, pp. 3318–3329, Jul. 2014.

[14] B. Wen, D. Boroyevich, R. Burgos, P. Mattavelli, and Z. Shen, "Analysis of D-Q small-signal impedance of grid-tied inverters," *IEEE Trans. Power Electron.*, vol. 31, no. 1, pp. 675–687, Jan. 2016.

[15] L. Harnefors, M. Bongiorno, and S. Lundberg, "Input-admittance calculation and shaping for controlled voltage-source converters," *IEEE Trans. Ind. Electron.*, vol. 54, no. 6, pp. 3323–3334, Dec. 2007.

[16] M. Cespedes and J. Sun, "Impedance modeling and analysis of grid-connected voltage-source converters," *IEEE Trans. Power Electron.*, vol. 29, no. 3, pp. 1254–1261, Mar. 2014.

[17] S. Skogestad and I. Postlethwaite, *Multivariable Feedback Control—Analysis and Design.* New York, NY, USA: Wiley, 2001.

[18] A. G. J. MacFarlane and I. Postlethwaite, "The generalized Nyquist stability criterion and multivariable root loci," *Int. J. Control*, vol. 25, no. 1, pp. 81–127, Feb. 1977.

[19] Z. Liu, J. Liu, W. Bao, and Y. Zhao, "Infinity-norm of impedance based stability criterion for three-phase AC distributed power systems with constant power loads," *IEEE Trans. Power Electron.*, vol. 30, no. 6, pp. 3030–3043, Jun. 2015.

[20] R. Rosso, G. Buticchi, M. Liserre, Z. Zou, and S. Engelken, "Stability analysis of synchronization of parallel power converters," in *Proc. 43rd Annu. Conf. IEEE Ind. Electron. Soc.*, Beijing, China, 2017, pp. 440–445.

[21] G. Buticchi, G. De Carne, D. Barater, Z. Zou, and M. Liserre, "Analysis of the frequency-based control of a master/slave micro-grid," *IET Renewable Power Gener.*, vol. 10, no. 10, pp. 1570–1576, 2016.

[22] A. Schwanka Trevisan, A. El-Deib, R. Gagnon, J. Mahseredjian, and M. Fecteau, "Field validated generic EMT-type model of a full converter wind turbine based on a gearless externally excited synchronous generator," *IEEE Trans. Power Del.*, vol. 33, no. 5, pp. 2284–2293, Oct. 2018, doi: 10.1109/TPWRD.2018.2850848.

[23] I. Postlethwaite and A. G. J. MacFarlane, *A Complex Variable Approach to the Analysis of Linear Multivariable Feedback System.* Berlin, Germany: Springer, 1979.

[24] K. Zhou and J. C. Doyle, *Essentials of Robust Control.* Englewood Cliffs, NJ, USA: Prentice-Hall, 1998.

[25] M. Belkhayat, "Stability criteria for AC power systems with regulated loads," Ph.D. dissertation, Dept. Elect. Comput. Eng., Purdue Univ., West Lafayette, IN, USA, 1997.

[26] A. Algassi, S. Perinpanayagam, M. Samie, and T. Sreenuch, "Computationally efficient, real-time, and embeddable prognostic techniques for power electronics," *IEEE Trans. Power Electron.*, vol. 30, no. 5, pp. 2623–2634, May 2015.

[27] H. Jedtberg, A. Pigazo, M. Liserre, and G. Buticchi, "Analysis of the robustness of transformerless PV inverter topologies to the choice of power devices," *IEEE Trans. Power Electron.*, vol. 32, no. 7, pp. 5248–5257, Jul. 2017.

[28] W. Li, *Risk Assessment of Power Systems: Models, Methods, and Applications.* Piscataway, NJ, USA: Wiley-IEEE Press, 2005.

[29] J. Rodriguez and P. Cortes, *Predictive Control of Power Converters and Electrical Drives.* Piscataway, NJ, USA: Wiley-IEEE Press, 2012.

[30] K. D. Young, V. I. Utkin, and U Oezguener, "A control engineer's guide to sliding mode control," *IEEE Trans. Control Syst. Technol.*, vol. 7, no. 3, pp. 328–342, May 1999.

[31] F. Wang, X. Mei, J. Rodriguez, and R. Kennel, "Model predictive control for electrical drive systems—An overview," *CES Trans. Elect. Mach. Syst.*, vol. 1, no. 3, pp. 219–230, Sep. 2017.

Roberto Rosso (S'17) received the B.Sc. degree in electronic engineering and the M.Sc. degree in electrical engineering from the University of Catania, Catania, Italy, in 2009 and 2012, respectively. Since 2017 he has been working toward the Ph.D. degree in electrical engineering at the Christian-Albrechts-University of Kiel, Kiel, Germany.

In 2013, he joined the R&D Division, Wind Turbine Manufacture ENERCON (Wobben Research and Development), Aurich, Germany, where he is currently with the Department of Control Engineering. He has been involved in several research projects addressing analytical models of electrical machines and control of electric drive systems. His research interest includes control strategies for grid integration of renewable energy systems.

Markus Andresen (S'15–M'17) received the M.Sc. degree in electrical engineering and business administration and the Ph.D. degree from the Chair of Power Electronics, Christian-Albrechts-University of Kiel, Kiel, Germany, in 2012 and 2017, respectively.

In 2010, he was an Intern with the Delta Shanghai Design Center, Delta Electronics Company, Ltd., Shanghai, China, and in 2017, he was a Visiting Scholar with the University of Wisconsin-Madison, Madison, WI, USA. His current research interests include control of power converters and reliability in power electronics.

Soenke Engelken (S'08–M'12) received the B.Sc. degree in electrical engineering and computer science from Jacobs University Bremen, Germany, in 2007, and the M.Sc. and the Ph.D. degrees in control engineering from the University of Manchester, Manchester, U.K., in 2008 and 2012, respectively.

He is currently the Head of the Department of Control Engineering, Wobben Research and Development, Aurich, Germany. The department develops control solutions for wind energy converters, spanning wind turbine controls, electrical systems controls, and grid-side converter controls.

Dr. Engelken is a member of the IEEE Power and Energy Society, the IEEE Control Systems Society, the CIGR Joint Working Group A1/C4.52 Wind Generators and Frequency-Active Power Control, and the ENTSO-E Expert Group on High Penetration Issues.

Marco Liserre (S'00–M'02–SM'07–F'13) received the M.Sc. and Ph.D. degree in electrical engineering from the Polytechnic University of Bari, Bari, Italy, in 1998 and 2002, respectively.

He was an Associate Professor with Polytechnic University of Bari and a Professor with Aalborg University, Denmark. He is currently a Full Professor and the Chair of Power Electronics with the Christian-Albrechts-University of Kiel, Kiel, Germany. He has authored and coauthored more than 300 technical papers (more than 86 of them in international peer-reviewed journals) and a book. These works have received more than 20 000 citations.

Dr. Liserre is listed in the ISI Thomson Report —The World's Most Influential Scientific Minds.